Article

Ultrathin, Porous CoPS Nanosheets: GO Self-Sacrificing Template Synthesis as Bifunctional Catalysts for Overall Water Splitting

Wenhua Zhao, Niandu Wu, Fan Yu, Boye Zhou, Xueyuan Chu, Zhiqiang Wei, and Shaoguang Yang*

Read Online

ACCESS | Metrics & More | Article Recommendations | SI Supporting Information

ABSTRACT: The exploitation of low-cost, porous, and ultrathin 2D electrocatalysts in the bifunctional electrocatalysis reaction and overall water splitting is a meaningful route to renewable energy technologies. Herein, as efficient bifunctional electrocatalysts toward the water-splitting process, the desirable cobalt phospho-sulfide (CoPS) nanosheets stem from Co^{2+} cross-linking to form strong coordination bonds with negatively charged oxygen-containing functional groups on a graphene oxide (GO) sacrificial template via electrostatic interactions. The prepared CoPS catalyst exhibits a distinguished electrochemical performance with a low overpotential (η) of hydrogen evolution reaction ($\sim$52 mV) and oxygen evolution reaction ($\sim$280.7 mV) at 10 mA cm^{-2} and better durability and higher turnover frequencies under alkaline environments. When it was used as the cathode and anode in alkaline media, the CoPS required only 1.62 V to achieve a current density of 10 mA cm^{-2}, outperforming most of the low-cost bifunctional electrocatalysts reported to date. The bond energy of the P=S bond not only effectively adsorb protons but also suitably weakens the adsorption on the Co−Co bridge site, thereby improving the multifunctional electrocatalysis for water splitting. The excellent performance of porous and ultrathin CoPS nanosheets is conducive to the complete exposure of active sites and facile ion transport kinetics, and they serve as a promising non-precious-metal-based electrocatalysts for the water-splitting reaction.

KEYWORDS: overall water splitting, bifunctional electrocatalyst, CoPS nanosheets, graphene oxide, sacrificial template
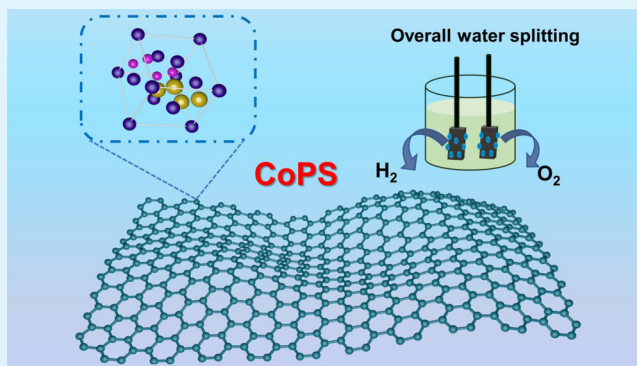
INTRODUCTION

Electrocatalytic water splitting possesses an environmentally benign and effective technology for renewable and clean energy production to relieve the energy shortage problem and environmental contamination. It proceeds via two half-cell reactions: an oxygen evolution reaction (OER) at the anode and a hydrogen evolution reaction (HER) at the cathode.[1] In the pursuit of inexpensive replacements for commercial electrocatalysts RuO_2/IrO_2 (OER) and Pt/C (HER), numerous nonprecious metals and their corresponding compounds as cost-effective and very efficient catalysts have roused the interest of researchers. Compared with noble-metal-based electrocatalysts (such as Pt, Ru, and Ir), non-noble-metal electrocatalysts exhibit superior electrochemical activities and stability. Recent research has focused on the development of cheap and efficient electrocatalysts, such as metal phosphides,[2,3] metal sulfides,[4,5] metal selenides,[6] oxides,[7] nitrides,[8] and so on. Among them, transition-metal phosphosulfides (MPSs)[9,10] represent an emerging electrocatalyst material that has been extensively investigated owing to its outperformed catalytic activity in comparison with the corresponding sulfide and phosphide counterparts. For instance, iron phosphosulfide nanoparticles on the surface possess higher P/S ratios, and the

P atoms suppress the oxidation of Fe and S atoms on the surface.[11] Cui and coworkers[12] reported that a Ni−P−S coating layer in a 3D graphene cage structure with a large specific surface area is developed for practical applications in Li−S batteries. Han[13] fabricated the MPS mixed with N-doped carbon nanotubes possessing noticeable HER activity.

Because cobalt has two oxidation states (Co II and Co III), the redox potential of Co is near the potential for oxygen reduction in water (1.23 V vs reversible hydrogen electrode (RHE)). This has made Co-based electrocatalysts more and more researched for the OER and HER. As early as the 1960s, new compounds with a cobaltite structure[14] were proposed by Hulliger. CoAsS is an example of these compounds, which has the same structure as FeS_2. In particular, cobalt phosphosulfide (CoPS) has the smallest lattice constant (a = 5.422 Å). In 2015, a ternary CoPS with a pyrite-type structure was
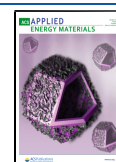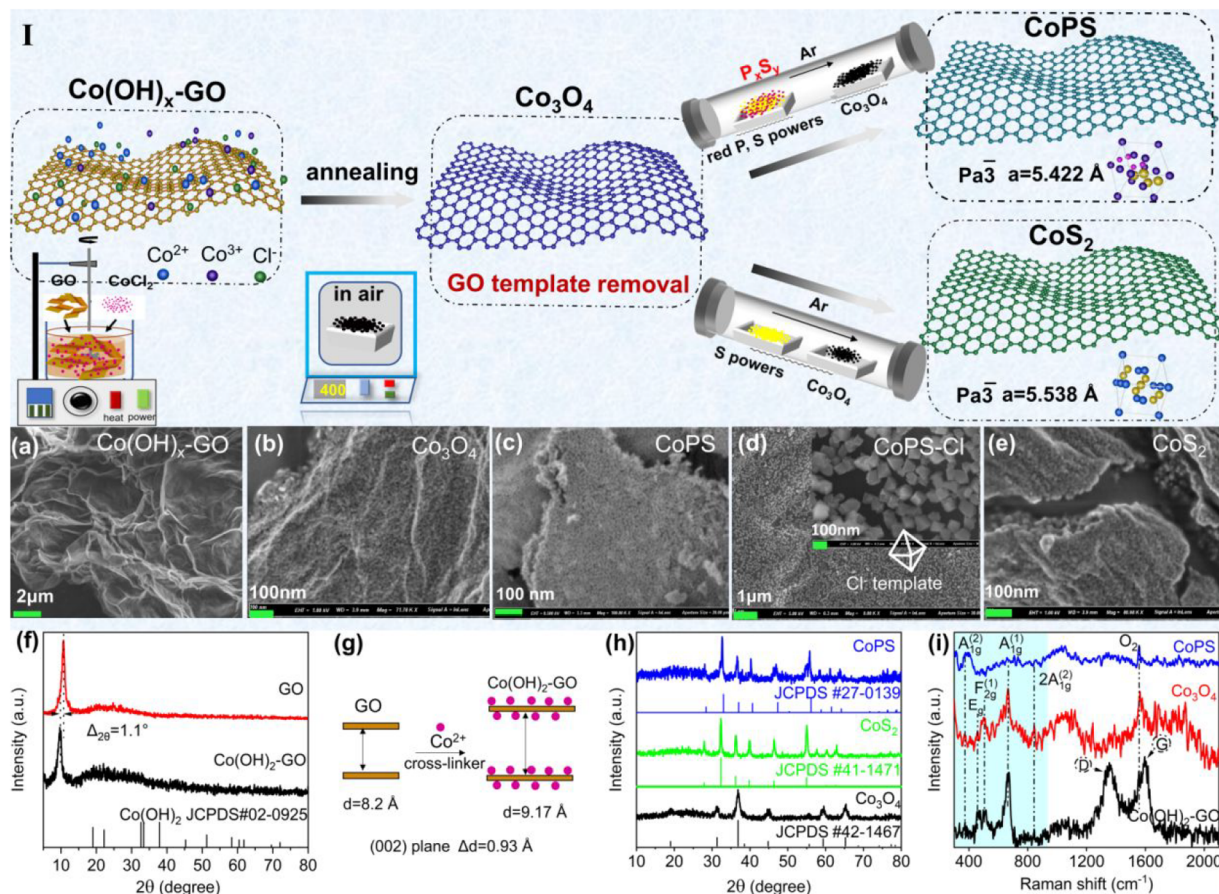
Figure 1. (I) Schematic illustration for the fabrication process and crystal structure of CoPS and CoS_2 catalysts. SEM images of (a) $Co(OH)_2$-GO, (b) Co_3O_4, (c) CoPS, (d) CoPS-Cl and (e) CoS_2 samples. XRD patterns of (f) GO and $Co(OH)_2$-GO and (h) Co_3O_4, CoS_2, and CoPS samples. (g) Schematic of cross-linking GO channels and the change in interlayer spacing. Co^{2+} is a cross-linker. (i) Raman characterization of $Co(OH)_2$-GO, Co_3O_4, and CoPS samples.

successfully synthesized first with superior catalytic activity for the HER.[15] The structure of CoPS is similar to that of CoS_2, whose lattice constant is slightly smaller than that of CoS_2 (a = 5.538 Å). The S^- ions of metallic CoS_2[16] are partially replaced by P^{2-} ions, forming the semiconductor CoPS. Because Co^{3+} mostly exists in CoPS, the adsorption of hydrogen can reduce Co^{3+} to Co^{2+} in the adjacent open P site and then oxidize Co^{2+} to Co^{3+} in the electrocatalytic process. The Co octahedron in CoPS contains a P^{2-} ligand, possessing higher electron-donating character than that of S^-, which is ascribed to the fact that more thermally neutral hydrogen can be adsorbed at the active site. Because high concentrations of H^+ and OH^- do not coexist in the electrolyte of the water-splitting cell,[17] it is imperative to construct the bifunctional electrocatalysts in the assembly of the cell and reduce the manufacturing cost accordingly. Recently, more research on MPS electrocatalysts for the OER and HER has been on the design, synthesis, and applications in alkaline electrolytes owing to their metalloid characteristics and superior electrical conductivity. A reasonable design of the electron and geometric structure of the catalyst can realize the rapid transfer and mass transfer of electrons.

Ultrathin 2D nanosheets with the cooperation of a large surface area, abundant active edges and rich defects will substantially promote catalyst performance. Designed on the basis of the characteristics of mild reaction conditions, well-defined 2D features, and porous architectures, the template-directed strategy was chosen to construct a 2D porous nanostructure by accelerating the lateral size control.[18−20] Owing to its negatively charged surface-oxygen-containing functional groups, graphene oxide (GO) was chosen as sacrifice template to form unique strong coordination bonds with cations. MPS nanosheets were also further synthesized by 2D metal oxide nanosheets, demonstrating the large electrochemically active surface area and greater number of active sites. Keeping these in consideration, the rational construction of 2D ultrathin CoPS nanosheets will have the potential of not only possessing abundant active sites but also greatly improving the structural stability of each component, thereby providing excellent electrocatalytic water splitting efficiency.

Herein the large-size, ultrathin CoPS nanosheets are synthesized with a GO self-sacrificing template by phospho-sulphur under the wet-chemical and chemical vapor deposition method. The CoPS nanosheets exhibit outstanding HER and OER electrocatalytic activity with extremely low overpotentials of 52 and 280.7 mV at a current density of 10 mA cm^{-2} in 1.0 M KOH, respectively, outperforming the CoS_2 and CoPS-Cl counterparts. Moreover, the fabricated CoPS nanosheets are regarded as bifunctional electrocatalysts for overall water splitting, which demonstrate an excellent stability with a low overpotential (∼1.62 V) to the required 10 mA·cm^{-2}.
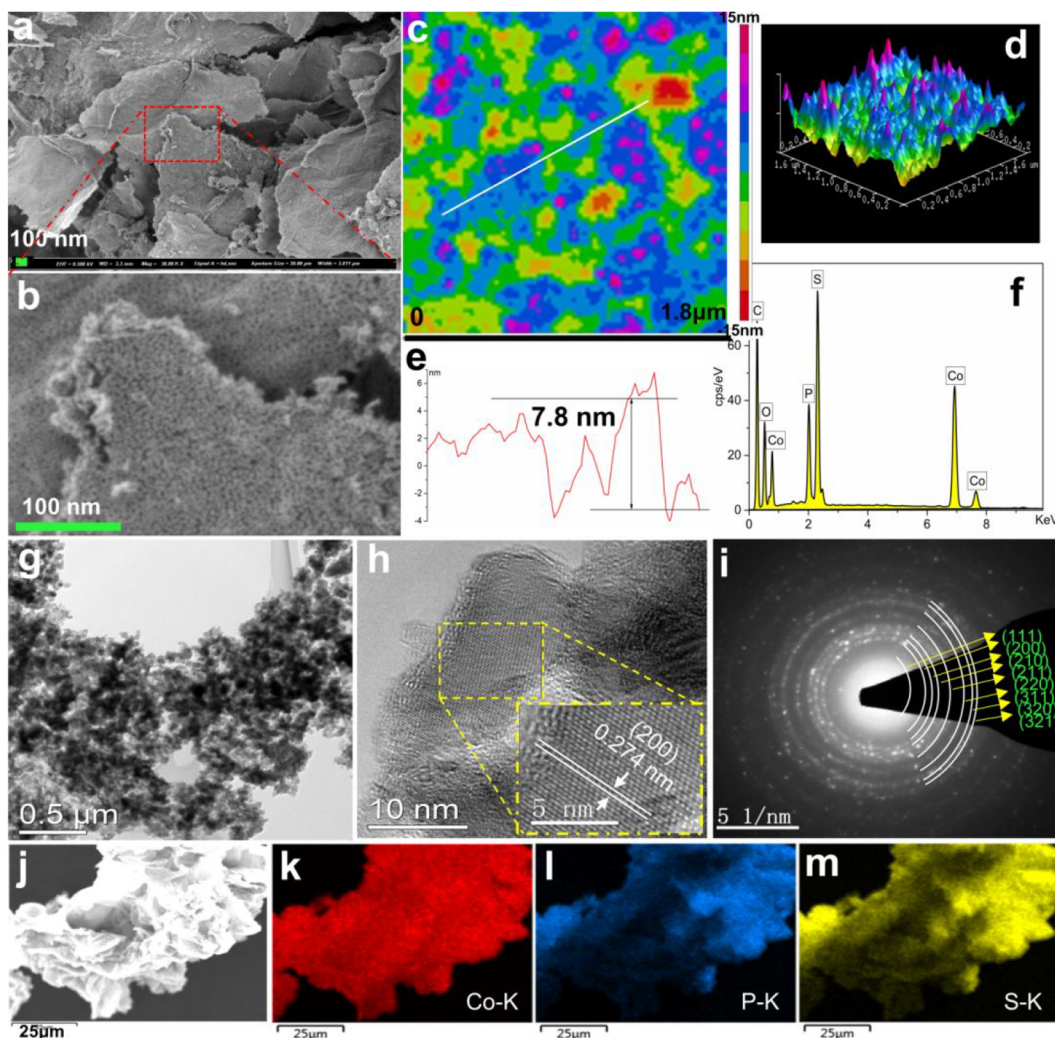
Figure 2. Morphology characterization of CoPS samples. (a,b) SEM images. (c−e) AFM image of CoPS sample. (f) EDS. (g) TEM. (h) HRTEM. (i) SAED. (j−m) Element mapping.

RESULTS AND DISCUSSION

The schematic illustration for the fabrication process of CoPS and CoS$_2$ catalysts is shown in Figure 1I. As cross-linkers and spacers for intercalation GO, the positively charged metal cations (Co^{2+}) can attract and finally attach on the surface and interlayers of GO to provide the corresponding hydroxide Co(OH)$_x$-GO by electrostatic attraction. Before metal ions adsorb on the surface of GO, it is necessary to reduce the hydrolysis of the metal ions as much as possible to avoid their nucleation, but it is required that the speed of the Co(OH)$_x$-GO hydrolysis is boosted after the adsorption process via regulation of the pH and temperature. As shown in Figure 1a, the morphology of Co(OH)$_2$-GO is inherited from that of GO nanosheets. From the X-ray diffraction (XRD) result in Figure 1f, the peak of Co(OH)$_2$-GO is shifted by 1.1° to a small angle compared with the peak of GO at 10.76° (corresponding to the (002) plane). This demonstrates that the layer spacing of GO template has increased by 0.93 Å along the C axis, as shown in Figure 1g. Co^{2+} can absorb negatively charged oxygen-containing functional groups at the interlayer and surface of GO nanosheets to form strong coordination bonds via electrostatic interactions, which should be responsible for the 1.1° shift. Subsequently, the porous, ultrathin, and large-size Co(OH)$_x$-GO nanosheets are converted to Co$_3$O$_4$ nanosheets by annealing in air to remove the GO template. In the synthetic procedure, it is critical to control the balance between the nucleation and growth of the Co$_3$O$_4$ precursor on the surface of GO. In Figure 1b, the large, ultrathin porous nanosheets stacked by nanoparticles of Co$_3$O$_4$ are demonstrated. It is further confirmed that the morphologies of CoPS (Figure 1c) and CoS$_2$ (Figure 1e) nanosheets are consistent with those of the precursor Co$_3$O$_4$ nanosheets. The GO self-sacrificing template strategy[21] mainly involves the uniform growth of Co$_3$O$_4$ on the surface of GO to form nanosheets; however, because of the existence of dual templates (GO template and Cl$^-$ template), the CoPS-Cl nanosheets in Figure 1d are covered with octahedral particles (∼100 nm) using the Co(OH)$_2$-Cl-GO precursor. It can be seen from Figure 1h that the peaks of Co$_3$O$_4$, CoS$_2$, and CoPS samples are well-indexed to JCPDS 42-1467, JCPDS 41-1471, and JCPDS 27-0139, respectively. We can implicitly confirm that the Co$_3$O$_4$, CoS$_2$, and CoPS samples with higher crystallinity are successful prepared without other impurity peaks. To further reveal the structure, we show the Raman characterization in Figure 1i. The peaks at 373.5, 458.4, 505.2, 663, and 843 cm^{-1} in the blue area correspond to A$_{1g}^{(2)}$, E$_g$, F$_{2g}^{(1)}$, A$_{1g}^{(1)}$, and 2A$_{1g}^{(2)}$, respectively. The appearance of these peaks confirms the
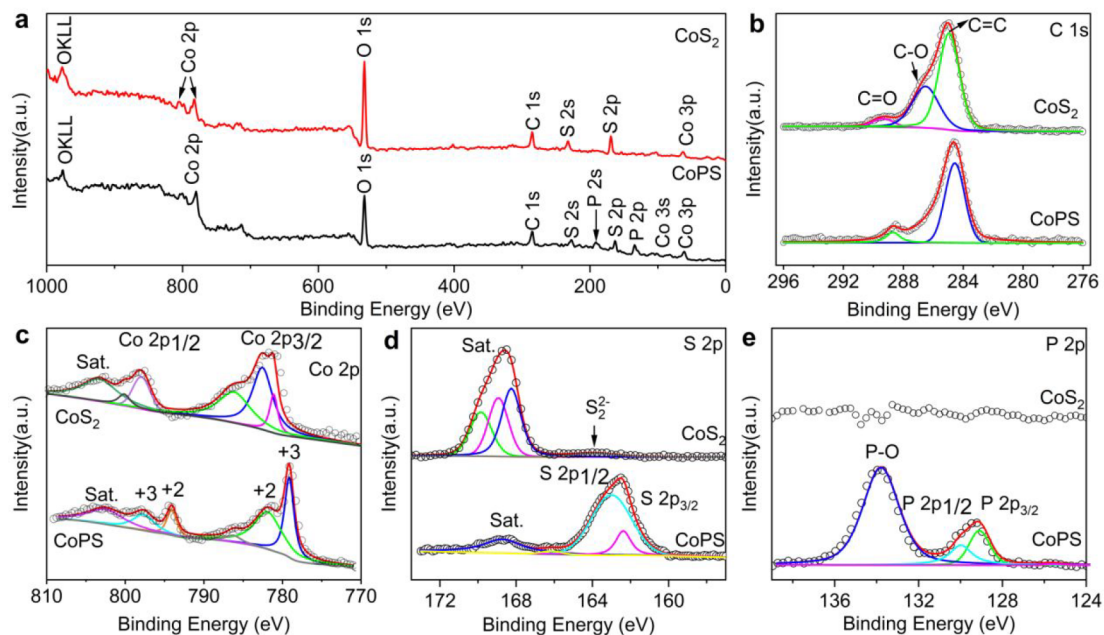
Figure 3. (a) XPS full spectrum. (b−e) High-resolution XPS spectra of C 1s, Co 2p, S 2p, and P 2p of CoS_2 and CoPS samples, respectively.

adsorption of Co(III).[22−25] In particular, the band at 373.5 cm^{-1} is attributed to the stretching vibration of the P−S bond.[26] The characteristic peak at 1556 cm^{-1} can be assigned to the presence of an O_2 molecule.[27] The 1354.7 and 1595.6 cm^{-1} peaks are the D band and the G band in the $Co(OH)_2$-GO sample, respectively. The intensity ratio of the D band to the G band (I_D/I_G = 0.936) can be used to characterize the degree of disorder in the crystal. The G band is related to the stretching vibration of the C atoms in the sp^2-hybridized plane, whereas the D band is generally caused by lattice defects in C atoms and may also be assigned to the random arrangement of graphite. Notably, the D peak and G peak disappeared in the Co_3O_4 and CoPS samples, demonstrating that the GO sacrificial template is successfully removed during the preparation process.

Meanwhile, the morphology of the synthesized CoPS sample is shown in Figure 2 using the GO self-sacrificing template. The ultrathin, large-size, and porous nanosheets are covered with uniform nanoparticles (5−12 nm) in the scanning electron microscopy (SEM) image (Figure 2a,b). The mapping of elements and the energy-dispersive X-ray spectroscopy (EDS) analysis of CoPS holey nanosheets in Figure 2j−m illustrate the uniform distribution of Co, P, and S. The atomic ratio of Co, P, and S elements is approximately 5.5:3.4:1.4. In the transmission electron microscopy (TEM) image in Figure 2g, CoPS nanosheets are still covered with many nanoparticles (~8 nm), consistent with the SEM results. The expected spacings of 0.274 nm for (200) lattice planes are displayed in the CoPS sample, which is indicative of the perfect crystallization with a 7−13 nm crystal grain, as shown in the high-resolution TEM (HRTEM) image (Figure 2h). The selected area electron diffraction (SAED) pattern of the CoPS nanosheets in the Figure 2i consists of many diffraction rings with different radii, corresponding to the (111), (200), (210), (211), (220), (311), (320), and (321) planes from interior to exterior, respectively. The corresponding planes are in agreement with that of JCPDS 27-0139 in the XRD result. The atomic force microscopy (AFM) images and the height

histograms of the CoPS nanosheets are employed to further determine the thickness. The corresponding height profiles (Figure 2d) demonstrate that the average thickness of the small-sized nanosheets is ~7.8 nm, well-matching with the SEM (Figure 2a) and TEM (Figure 2g) images. Notably, there are many holes (diameter is 5−15 nm) on the ultrathin CoS_2 nanosheets, depicted in Figure S1a. The d-spacing value in the clear lattice fringe of HRTEM (Figure S1b) is 0.28 nm, corresponding to the (200) plane of the CoS_2. It further illustrates that the porous CoS_2 nanosheets consist of nanoparticles (~6 nm). All polycrystalline diffraction rings in SAED can be indexed in terms of the CoS_2, which implies that the CoS_2 nanosheets remain well-crystallized. It is critical that the use of a GO self-sacrificing template for the preparation of nanomaterials is a facile method to design and construct 2D porous and ultrathin nanosheets.

Surface analysis of the chemical states of elements in the composite are carried out on CoS_2 and CoPS via X-ray photoelectron spectroscopy (XPS). The XPS full spectra of CoS_2 and CoPS are shown in Figure 3a. Figure 3b−e shows the high-resolution XPS spectra of C 1s, Co 2p, S 2p, and P 2p, respectively. Taking the C peak (284.8 eV) as a benchmark, it can be seen that the peak of C 1s in the XPS has shifted to low binding energy by ~0.3 (CoS_2 284.5 eV) and 0.2 eV (CoPS 284.6 eV), respectively. The XPS-induced Auger peak (OKLL) is located at 976.3 eV.[28] The high-resolution XPS spectra of Co 2p (Figure 3c) show two-part peaks centered around 782 and 797 eV, corresponding to Co $2p_{1/2}$ and Co $2p_{3/2}$, respectively.[29] The coexistence of Co^{3+} in the CoS_2 catalyst is observed on the peak at 798.1 eV. Other peaks at 781.3 and 782.9 eV are assigned to +2 state of Co. In addition, the Co $2p_{3/2}$ peak in the CoPS sample is deconvolved into two peaks (782.2 and 779.35 eV), which can be ascribed to Co^{2+} and Co^{3+}, respectively.[30] Other peaks of Co $2p_{1/2}$ are located at 794.33 and 797.8 eV, assigned to the Co^{2+} and Co^{3+} states.[31] Meanwhile, the S $2p_{3/2}$ and S $2p_{1/2}$ peaks in S 2p are located at 162.5 and 163.25 eV from CoPS (Figure 3d), respectively, corresponding to the S^{2-} state. A small peak in CoS_2 is
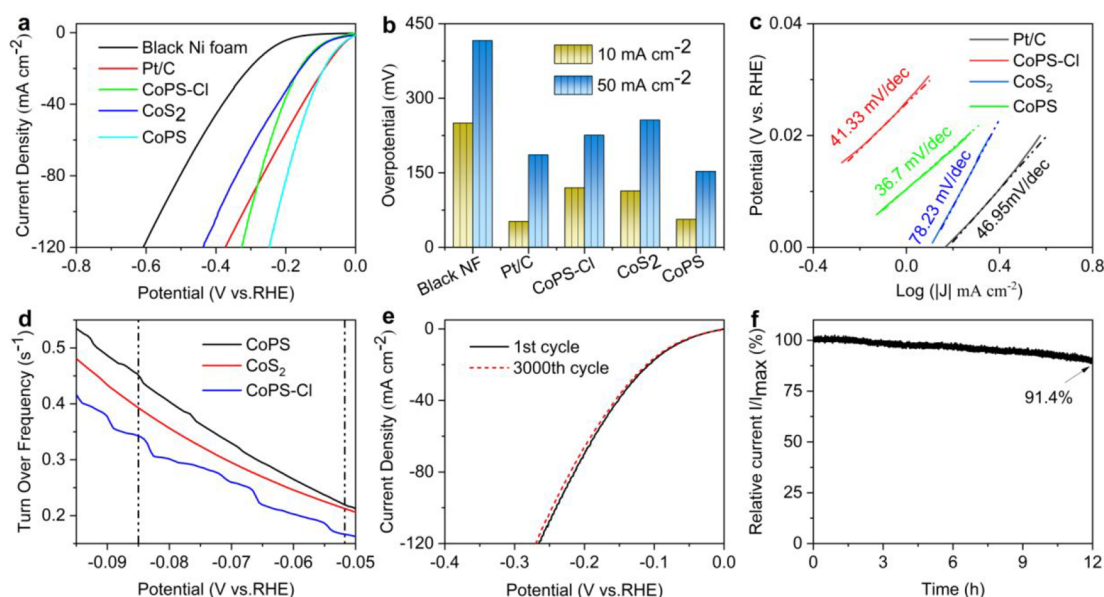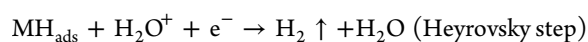
Figure 4. (a) Polarization curves for the HER. (b) Overpotential at 10 and 50 mA·cm^{-2} of the 20% Pt/C, CoPS-Cl, CoS$_2$, and CoPS electrodes and (c) corresponding Tafel plots. (d) Turnover frequency of the CoPS-Cl, CoS$_2$, and CoPS electrodes. (e) LSV curves of CoPS before and after 3000 CV cycles. (f) Time-dependent chronoamperometry curves at overpotential at 52 mV for 12 h of CoPS sample.

consistent with S$_{2-2}$, located at 164.2 eV.[32] The P 2p spectrum is divided into two peaks positioned at 129.5 and 130.41 eV in Figure 3e, distributed to P 2p$_{3/2}$ and P 2p$_{1/2}$ in CoPS.[33] Meanwhile, the peak at 134.16 eV corresponds to the P−O bond.[34] An optimized electronic environment with an electron coupling effect between the Co−S, Co−P, and P=S bonds is expected to improve the intrinsic activity in the OER and HER.
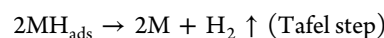
We measured Co-based electrocatalysts in the three-electrode system with an electrolyte of 1 M KOH to obtain the intrinsic activity of electrocatalysis. The Ag/AgCl electrode was used as a reference electrode, and a graphite rod was used as counter electrode. Meanwhile, the catalysts were loaded on Ni foam (1*1 cm) as a working electrode, respectively. The polarization curves exhibit the normalized current density, j, versus the voltage, V, for the CoPS, CoS$_2$, and CoPS-Cl electrodes along with the reference black Ni foam and commercial 20% Pt/C for comparison. The CoPS nanosheets show significantly excellent HER performance with a low overpotential of 52 mV at 10 mA cm^{-2} (Figure 4a), whereas black Ni foam, CoPS-Cl, and CoS$_2$ reveal an overpotential of over 250, 119.57, and 113.49 mV to achieve 10 mA cm^{-2}, respectively. Despite the fact that the onset potential of commercial 20% Pt/C is close to zero, its overpotential is still weaker than that of CoPS at a high current density. Characterized by η = 186 mV at a current density of 50 mA cm^{-2}, the CoPS nanosheets behave as an excellent hydrogen evolution cathode. When the applied potential is higher than −93.9 mV, the performance of CoPS is much better than 20% Pt/C in the RHE. Tafel slopes for all catalysts are calculated in Figure 4c. The following steps are the accepted steps by which cathodic H$_2$ evolution occurs at various metals, M, involving an adsorbed H intermediate, M−H$_{ads}$

$$H_3O^+ + e^- + M \rightarrow MH_{ads} + H_2O \text{ (Volmer step)}$$

followed by either

$$MH_{ads} + H_2O^+ + e^- \rightarrow H_2 \uparrow + H_2O \text{ (Heyrovsky step)}$$

or

$$2MH_{ads} \rightarrow 2M + H_2 \uparrow \text{ (Tafel step)}$$

In general, the Volmer (electrochemical hydrogen adsorption), Heyrovsky (electrochemical desorption), or Tafel step (chemical desorption) is the rate-determining step. In an alkaline solution or for pH values greater than ~5, H$_2$O itself is the the proton source, leading to OH$^-$ as the conjugate-base product after electron transfer.[35] According to the kinetic models, the Tafel slopes of the above steps are expected to be about 120, 40, and 30 mV dec^{-1}, respectively. The Tafel slope of the CoPS nanosheets is 36.7 mV/dec, which is markedly smaller than those of CoPS-Cl (41.33 mV/dec) and CoS$_2$ (78.23 mV/dec). Because the Tafel slope of CoPS approaches 40 mV dec^{-1}, the electrocatalytic HER kinetics is decided by the Volmer−Heyrovsky mechanism.[36] The intrinsic activity of the CoPS nanosheets is further evaluated by the turnover frequency (TOF). The CoPS sample exhibits the largest value of TOF of 0.452 and 0.2217 s^{-1} (at an overpotential of 85 and 52 mV) among the Co-based electrocatalysts, which is much larger than those of the corresponding CoS$_2$ (0.34 and 0.213 s^{-1}) and CoPS-Cl (0.39 and 0.167 s^{-1}). Furthermore, the η at 10 mA cm^{-2} against the Tafel slopes of CoPS and previously reported catalysts is plotted in Figure S3, which indicates that the as-prepared CoPS exhibits outstanding HER activity. The results demonstrate that the species of anion and the particle size of the sample can determine the kinetics of hydrogen evolution. Compared with metal sulfides, MPSs can improve the desorption capacity for H$_{ads}$ species of the electrocatalyst. At the same time, the center of the crystal surface of the MPS cut off by P=S is negatively charged. These sites can effectively adsorb protons, making them discharge, and promote the hydrogen absorption reaction.[37,38] The bond energy of the P=S bond (335 kJ/mol) is between the P−H bond (322 kJ/mol) and the S−H bond (363 kJ/mol), which suitably weakens the adsorption on the Co−Co bridge site, thereby improving the hydrogen absorption performance.[39] The stability is another indispensable indicator of the
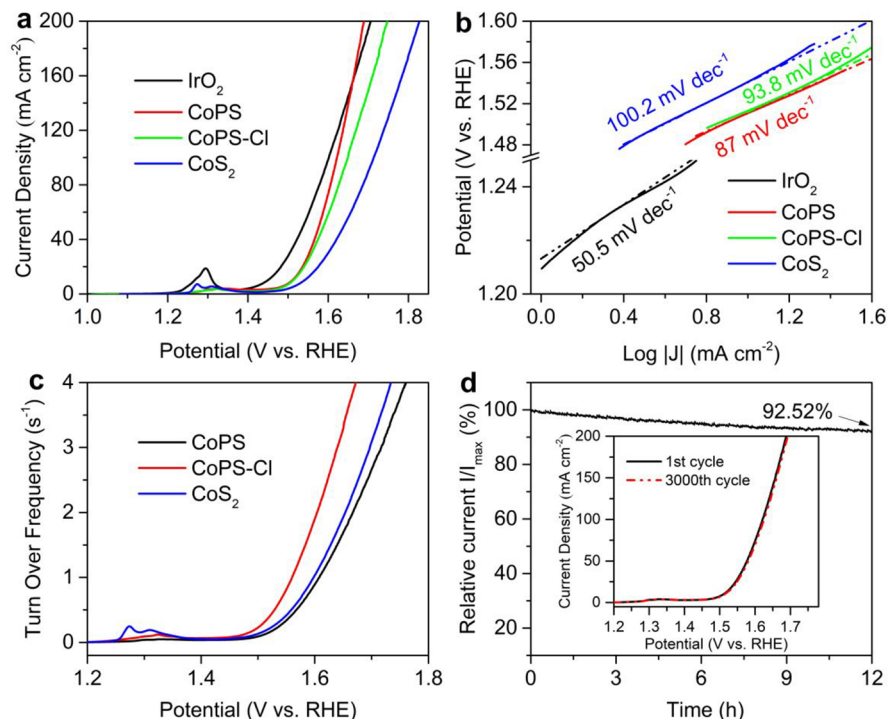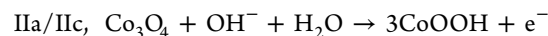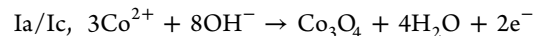
Figure 5. (a) Polarization curves for the OER and (b) corresponding Tafel plots of the IrO$_2$, CoPS-Cl, CoS$_2$, and CoPS electrodes. (c) Turnover frequency of the CoPS-Cl, CoS$_2$, and CoPS electrodes. (d) Time-dependent chronoamperometry curves at overpotential at 280.71 mV for 12 h and LSV curves before and after 3000 CV cycles of CoPS sample (insert).

electrocatalyst for evaluating the catalytic activity. The linear sweep voltammetry (LSV) of the CoPS for the HER activity after 3000 CV cycles has only slight distinction (Figure 4e). Furthermore, time-dependent chronoamperometry (CP) curves at η = 52 mV for 12 h of the CoPS sample are shown in Figure 4f. Obviously, the current density of CoPS attenuates to only 91.4% relative to the initial test. The XRD and morphology of CoPS nanosheets after the HER long-term test (Figure S2a−c) are negligible compared with those of the initial test, implying its good stability for the HER.

The OER performances of CoPS-Cl, CoS$_2$, CoPS, and IrO$_2$ deposited in Ni foam with similar mass loading levels are compared (Figure 5a) in 1 M KOH electrolyte. Notably, investigated as a commercially available catalysts for the OER, IrO$_2$ exhibits optimal activity with a low overpotential of 219.53 mV to achieve 10 mA cm^{-2}, whereas the black Ni foam reveals poor catalytic performances. When the current density increases to 154 mA, the overpotential of CoPS nanosheets is gradually lower than that of IrO$_2$. Moreover, the CoPS nanosheets behave as an efficient oxygen evolution cathode, characterized by an overpotential of 280.7 mV at 10 mA cm^{-2}. The present overpotential of the CoPS for the OER (Table S1) is also substantially lower than that recently reported for non-noble-metal electrocatalysts at 10 mA cm^{-2}. As shown in Figure 5b, the Tafel plots of the IrO$_2$, CoPS-Cl, CoS$_2$, and CoPS electrodes are 50.5, 93.8, 100.2, and 87 mV·dec^{-1}, respectively; however, the TOF of the CoPS is inferior to those of CoS$_2$ and CoPS-Cl electrodes. When CoPS is used as the catalyst for the OER after the 3000 CV cycles test, its LSV curve remains almost unchanged, even in the inset of Figure 5d. In addition, the current density barely decreases (only 7.48%), indicating that the electrode can maintain a steady activity over a period of 12 h. Notably, the superior durability of the IrO$_2$ catalyst exhibits severe polarization after 7 h tests in

Figure S4, which was similarly reported in previous literature.[40,41] Compared with the initial CoPS, the morphological integrity and XRD result confirm the stability of the CoPS sample after a long-term test of the OER for 12 h in Figure S2d−f.

The direct change process of Co^{2+}, Co^{3+}, and Co^{4+} in Co$_3$O$_4$ can be derived from the oxidation peaks in the cyclic voltammogram (CV) curve, which are recorded in 1 M KOH with CoPS (Figure S5). Co^{3+} is often considered as the active site in the OER process. The redox couples Ia/Ic and IIa/IIc at ∼0.75 to 1.05 V and 1.06 to 1.27 V can be ascribed to the transformation between Co(II) and Co(III), respectively. No obvious IIa peak as a CoOOH surface layer in Co$_3$O$_4$ was spontaneously formed in alkaline electrolyte.[42] Another pair of redox peaks, IIIa/IIIc, in the range of ∼1.29 to 1.5 V can be assigned to the Co(III)/Co(IV) redox couple. The three sets of redox couples are involved as follows[43]

$$\text{Ia/Ic,} \quad 3\text{Co}^{2+} + 8\text{OH}^- \rightarrow \text{Co}_3\text{O}_4 + 4\text{H}_2\text{O} + 2\text{e}^-$$

$$\text{IIa/IIc,} \quad \text{Co}_3\text{O}_4 + \text{OH}^- + \text{H}_2\text{O} \rightarrow 3\text{CoOOH} + \text{e}^-$$

$$\text{IIIa/IIIc,} \quad \text{CoOOH} + \text{OH}^- \rightarrow \text{CoO}_2 + \text{H}_2\text{O} + \text{e}^-$$

Obviously, the intensity of the IIIa peak represents the evolution of electrochemical oxygen. At this time, Co(III) of the surface is oxidized to Co(IV), which demonstrates that Co(IV) is crucial for the OER.[40] To further understand the influence of the Co(III)/Co(IV) redox couple on the OER, we illustrate the proposed OER reaction process on the CoPS surface in the following steps[44]
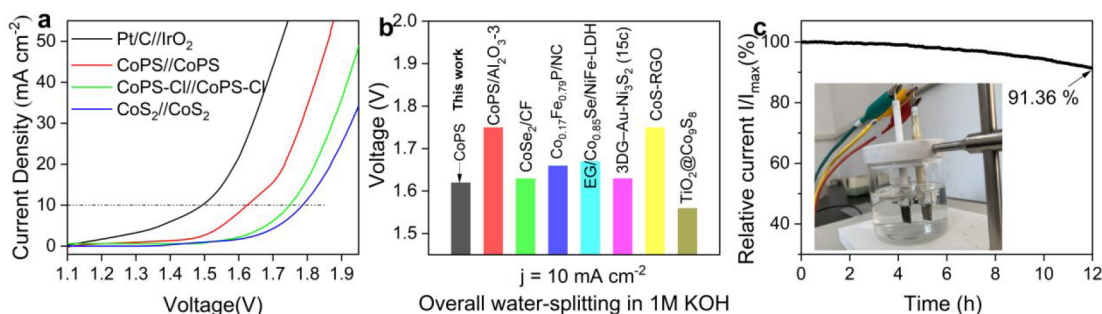
$$\text{M} + \text{OH}^- \rightarrow \text{MOH} + \text{e}^- \tag{1}$$

$$\text{MOH} + \text{OH}^- \rightarrow \text{MO} + \text{H}_2\text{O} + \text{e}^- \tag{2}$$
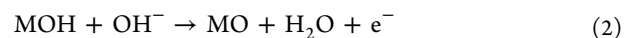
Figure 6. (a) Polarization curves of Pt/C//IrO$_2$, CoPS-Cl//CoPS-Cl, CoS$_2$//CoS$_2$, and CoPS//CoPS for overall water splitting obtained in 1 M KOH solution with a scan rate of 2 mV s^{-1} at room temperature. (b) Comparison of the cell voltages in 1 M KOH to drive a current density of 10 mA cm^{-2} for the CoPS with recently reported TM-based bifunctional catalysts. (c) Time-dependent chronoamperometry curves at an overpotential 1.62 V for 12 h of CoPS//CoPS.

$$MO + OH^- \rightarrow MOOH + e^- \qquad (3)$$

$$MOOH + OH^- \rightarrow M + O_2 + H_2O + e^- \qquad (4)$$
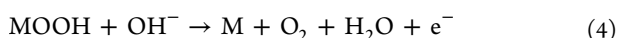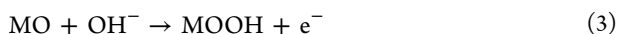
In the OER process, the more active Co^{3+} sites can produce the adsorption of reactive species (e.g., OH, O, OOH, etc.).[45,46] Thereby, these reduce the OER charge-transfer resistance. When surface Co^{3+} is oxidized to Co^{4+}, the electrophilicity of the intermediate makes the nucleophilic species OH$^-$ react with it, which further accelerates the formation of A−OOH$_{ads}$. In addition, the IIc peak in Figure S5 obviously shows that CoOOH is reduced to Co(III).[47] By the electron-withdrawing inductive effect, Co^{4+} can finally strengthen the deprotonation of A−OOH$_{ads}$ to form the product O$_2$. Thus Co-based materials are considered as precatalysts for the formation of oxide/hydroxide catalysts, and M−OOH is supposed as a highly active phase.[48]

Electrochemical impedance spectroscopy (EIS, Figure S6) is performed at overpotentials of −0.52 V for the HER and 1.5107 V for the OER in a 1 M KOH solution. The variance in the charge-transfer resistances (R_{ct}) is derived from the semicircles in the low range of Nyquist plots.[49] CoPS demonstrates the fastest charge-transfer process during the water electrolysis of electrocatalysts because of its smallest R_{ct} (0.08 Ω for the OER and 0.16 Ω for the HER, respectively). The N$_2$ adsorption−desorption isotherm of the CoPS nanosheets is observed in Figure S7. It shows the BET specific surface area of the CoPS nanosheets is 39.57 m^2/g. Notably, the hysteresis loop in the P/P_0 is range of 0.55−1.0, which indicates that typical mesoporous structure.[50] The pore diameters is clearly distributed between 2 and 20 nm is indicative of electric double layer development and accelerated ions transfer is shown in the inset of Figure S7. The total pore volume was 0.022 cm^3/g. The high surface area of CoPS provides a high surface exposure of active sites for the electrocatalyst. Considering the fact that the double-layer capacitance (C_{dl}) is proportional to the electrochemically active surface area (ECSA), C_{dl} could be calculated to evaluate the electrochemical active area. The CV curves of the electrode are measured at intervals of 0.1 V width in the non-Faraday region. The C_{dl} values are calculated via plotting the slope (k) of $\Delta j = j_a - j_c$ at a middle potential (vs RHE) against the different sweep scan rates (20−200 mV s^{-1}). The C_{dl} value is half of the slope of the curve, whereas $C_{dl} = 0.5k$. As shown in Figure S8d, the C_{dl} value for the CoPS electrode (2.87 mF cm^{-2}) is 2.7 times higher than those of CoPS-Cl (1.07 mF cm^{-2}) and CoS$_2$ (1.06 mF cm^{-2}). Improving the efficient mass diffusion and anion exchangeability, the high C_{dl} value of CoPS

nanosheets corresponds to the high ECSA, which might be attributed to its ultrathin and porous morphology. In the presence of Cl$^-$, CoPS-Cl presents octahedral particles with large size (>100 nm), and no ultrathin, porous structure appears. Therefore, both the specific surface area and ECSA of CoPS-Cl are smaller than those of CoPS, resulting in the decrease in the catalytic performance. To evaluate the faradic efficiency of the HER and OER, we collected the H$_2$ and O$_2$ produced during electrolysis at 10 mA cm^{-2} for 60 min via the drainage gas collection method. As shown in Figure S9, the collected H$_2$ and O$_2$ always maintain a 2:1 stoichiometric ratio. The Faraday efficiencies of CoPS for the OER and HER processes are close to 98.9 and 97.8%, respectively.

Inspired by the superior catalytic performance of the CoPS nanosheets on Ni foam for the OER and HER, we assembled CoPS as the anode and the cathode to simulate real water electrolysis in alkaline electrolyte, as shown in the inset of Figure 6c. The electrolyzers with structures of Pt/C//IrO$_2$, CoPS-Cl//CoPS-Cl, and CoS$_2$//CoS$_2$ were prepared for comparison, respectively. Figure 6a displays the LSV curves of all of the electrocatalysts for the OER. The CoPS//CoPS electrolyzer exhibits the lowest cell voltage of 1.62 V, which is superior to those of the CoPS-Cl//CoPS-Cl (1.749 V) and CoS$_2$//CoS$_2$ (1.78 V) electrolyzers. Impressively, CoPS nanosheets demonstrate a voltage of 1.62 V at a current density of 10 mA cm^{-2}, which is substantially lower than those of the CoPS/Al$_2$O$_3$-3||CoPS/Al$_2$O$_3$-3 catalyzer cell (1.75 V)[51] and reported electrocatalysts such as CoSe$_2$/CF[52] (1.63 V), Co$_{0.17}$Fe$_{0.79}$P/NC (1.66 V),[33] EG/Co$_{0.85}$Se/NiFe-LDH (1.67 V),[53] 3DG-Au-Ni$_3$S$_2$ (15c) (1.63 V),[54] and CoS-RGO (1.75 V)[55] (Figure 6b) and is even close to those of the Pt/C||IrO$_2$ (1.49 V) and TiO$_2$@Co$_9$S$_8$ (1.56 V)[56] catalyzer cells. Furthermore, the long-term stability of the CoPS//CoPS electrolyzer was evaluated by time-dependent CP curves at an overpotential of 1.62 V for 12 h, which illustrates that the relative current of CoPS//CoPS remains 91.36% after 12 h of continuous electrolysis (Figure 6c). The superior overall water-splitting performance of CoPS//CoPS is mainly ascribed to the following advantages: (i) There are generally enhanced structural stability and catalytic activity ascribed to the synergy between different components in ternary compounds.[57,58] (ii) The GO self-sacrificing template can improve the ECSA, further enhancing the number of active sites. Porous and ultrathin CoPS nanosheets could facilitate the diffusion of ions and electron transport and suppress the aggregation of active species during the electrolysis.[53,59] Notably, we implicitly conclude that the GO self-sacrificing template method

selectively maintains the integrity of morphology to improve the catalysis performance of water electrolysis.

CONCLUSIONS

In summary, porous and ultrathin CoPS nanosheets were successfully prepared using GO as template via a facile wet-chemical and chemical vapor deposition process. The prepared CoPS nanosheets covered with uniform particles (5−12 nm) achieved outstanding electrocatalytic performance, showing very low overpotentials of 52 mV for the HER and 280.7 mV for the OER at a current density of 10 mA cm^{-2} in 1.0 M KOH, respectively. Additionally, the CoPS nanosheets exhibited an ultralow applied 1.62 V at 10 mA cm^{-2} for overall water splitting and maintained the distinguished performance during a long-term stability test. We implicitly conclude that CoPS ternary compounds with synergistic effects demonstrate that the P=S bond effectively adsorbs protons and weakens the Co−Co bridge site in the HER. The Co^{3+} sites could better adsorb reactive species to reduce the OER charge-transfer resistance, thereby improving the electro-catalysis performance. Critically, this facile strategy for preparing 2D porous and ultrathin CoPS nanosheets can further inspire the design and construction of more efficient nonprecious catalysts.

ASSOCIATED CONTENT

ⓈⒾ Supporting Information

The Supporting Information is available free of charge at https://pubs.acs.org/doi/10.1021/acsaem.1c01929.

> Figures of XRD, SEM, TEM, and HRTEM images; CV curves and scan rate fitted to a linear regression allow for the estimation of C_{dl}; N_2 adsorption−desorption isotherm of CoPS; comparison of the overpotential at a current density of 10 mA cm^{-2} and Tafel slope on various HER- and OER-active cobalt phosphide and sulfide-based electrocatalysts; Faradaic efficiency of CoPS for HER and OER (PDF)

AUTHOR INFORMATION

Corresponding Author

Shaoguang Yang − School of Physics, National Laboratory of Solid State Microstructures, Collaborative Innovation Center of Advanced Microstructures, Nanjing University, Nanjing 210093, China; Email: sgyang@nju.edu.cn

Authors

Wenhua Zhao − School of Physics, National Laboratory of Solid State Microstructures, Collaborative Innovation Center of Advanced Microstructures, Nanjing University, Nanjing 210093, China; ⓞ orcid.org/0000-0002-9009-6119

Niandu Wu − School of Physics, National Laboratory of Solid State Microstructures, Collaborative Innovation Center of Advanced Microstructures, Nanjing University, Nanjing 210093, China

Fan Yu − School of Physics, National Laboratory of Solid State Microstructures, Collaborative Innovation Center of Advanced Microstructures, Nanjing University, Nanjing 210093, China

Boye Zhou − School of Physics, National Laboratory of Solid State Microstructures, Collaborative Innovation Center of Advanced Microstructures, Nanjing University, Nanjing 210093, China

Xueyuan Chu − School of Physics, National Laboratory of Solid State Microstructures, Collaborative Innovation Center of Advanced Microstructures, Nanjing University, Nanjing 210093, China

Zhiqiang Wei − School of Science, Lanzhou University of Technology, Lanzhou 730050, China

Complete contact information is available at:
https://pubs.acs.org/10.1021/acsaem.1c01929

Author Contributions

The manuscript was written through contributions of all authors. All authors have given approval to the final version of the manuscript.

Notes

The authors declare no competing financial interest.

ACKNOWLEDGMENTS

REFERENCES

(1) Qiu, Y.; Zhang, X.; Han, H.; Liu, Z.; Liu, J.; Ji, X. Advantageous Metal-Atom-Escape towards Super-Hydrophilic Interfaces Assembly for Efficient Overall Water Splitting. *J. Power Sources* **2021**, *499*, 229941.

(2) Bao, J.; Zhou, Y.; Zhang, Y.; Sheng, X.; Wang, Y.; Liang, S.; Guo, C.; Yang, W.; Zhuang, T.; Hu, Y. Engineering Water Splitting Sites in Three-Dimensional Flower-like Co−Ni−P/MoS$_2$ Heterostructural Hybrid Spheres for Accelerating Electrocatalytic Oxygen and Hydrogen Evolution. *J. Mater. Chem. A* **2020**, *8* (42), 22181−22190.

(3) Fu, Q.; Wu, T.; Fu, G.; Gao, T.; Han, J.; Yao, T.; Zhang, Y.; Zhong, W.; Wang, X.; Song, B. Skutterudite-Type Ternary Co$_{1-x}$Ni$_x$P$_3$ Nanoneedle Array Electrocatalysts for Enhanced Hydrogen and Oxygen Evolution. *ACS Energy Lett.* **2018**, *3* (7), 1744−1752.

(4) Guo, Y.; Tang, J.; Wang, Z.; Kang, Y.-M.; Bando, Y.; Yamauchi, Y. Elaborately Assembled Core-Shell Structured Metal Sulfides as a Bifunctional Catalyst for Highly Efficient Electrochemical Overall Water Splitting. *Nano Energy* **2018**, *47*, 494−502.

(5) Zhao, M.; Li, W.; Li, J.; Hu, W.; Li, C. M. Strong Electronic Interaction Enhanced Electrocatalysis of Metal Sulfide Clusters Embedded Metal−Organic Framework Ultrathin Nanosheets toward Highly Efficient Overall Water Splitting. *Adv. Sci.* **2020**, *7* (20), 2001965.

(6) Fang, Z.; Peng, L.; Qian, Y.; Zhang, X.; Xie, Y.; Cha, J. J.; Yu, G. Dual Tuning of Ni−Co−A (A = P, Se, O) Nanosheets by Anion Substitution and Holey Engineering for Efficient Hydrogen Evolution. *J. Am. Chem. Soc.* **2018**, *140* (15), 5241−5247.

(7) Kuang, M.; Han, P.; Wang, Q.; Li, J.; Zheng, G. CuCo Hybrid Oxides as Bifunctional Electrocatalyst for Efficient Water Splitting. *Adv. Funct. Mater.* **2016**, *26* (46), 8555−8561.

(8) Sun, H.; Tian, C.; Fan, G.; Qi, J.; Liu, Z.; Yan, Z.; Cheng, F.; Chen, J.; Li, C.-P.; Du, M. Boosting Activity on Co$_4$N Porous Nanosheet by Coupling CeO2 for Efficient Electrochemical Overall Water Splitting at High Current Densities. *Adv. Funct. Mater.* **2020**, *30* (32), 1910596.

(9) Kibsgaard, J.; Jaramillo, T. F. Molybdenum Phosphosulfide: An Active, Acid-Stable, Earth-Abundant Catalyst for the Hydrogen Evolution Reaction. *Angew. Chem., Int. Ed.* **2014**, *53* (52), 14433−14437.

(10) Liu, W.; Hu, E.; Jiang, H.; Xiang, Y.; Weng, Z.; Li, M.; Fan, Q.; Yu, X.; Altman, E. I.; Wang, H. A Highly Active and Stable Hydrogen Evolution Catalyst Based on Pyrite-Structured Cobalt Phosphosulfide. *Nat. Commun.* **2016**, *7* (1), 10771.

(11) Wu, Z.; Li, X.; Liu, W.; Zhong, Y.; Gan, Q.; Li, X.; Wang, H. Materials Chemistry of Iron Phosphosulfide Nanoparticles: Synthesis,

Solid State Chemistry, Surface Structure, and Electrocatalysis for the Hydrogen Evolution Reaction. *ACS Catal.* **2017**, 7 (6), 4026−4032.

(12) Zhou, G.; Sun, J.; Jin, Y.; Chen, W.; Zu, C.; Zhang, R.; Qiu, Y.; Zhao, J.; Zhuo, D.; Liu, Y.; Tao, X.; Liu, W.; Yan, K.; Lee, H. R.; Cui, Y. Sulfiphilic Nickel Phosphosulfide Enabled Li$_2$S Impregnation in 3D Graphene Cages for Li−S Batteries. *Adv. Mater.* **2017**, 29 (12), 1603366.

(13) Li, D. J.; Kang, J.; Lee, H. J.; Choi, D. S.; Koo, S. H.; Han, B.; Kim, S. O. High Activity Hydrogen Evolution Catalysis by Uniquely Designed Amorphous/Metal Interface of Core-Shell Phosphosulfide/N-Doped CNTs. *Adv. Energy Mater.* **2018**, 8 (13), 1702806.

(14) Hulliger, F. New Compounds with Cobaltite Structure. *Nature* **1963**, 198 (4878), 382−383.

(15) Cabán-Acevedo, M.; Stone, M. L.; Schmidt, J. R.; Thomas, J. G.; Ding, Q.; Chang, H.-C.; Tsai, M.-L.; He, J.-H.; Jin, S. Efficient Hydrogen Evolution Catalysis Using Ternary Pyrite-Type Cobalt Phosphosulphide. *Nat. Mater.* **2015**, 14 (12), 1245−1251.

(16) Faber, M. S.; Dziedzic, R.; Lukowski, M. A.; Kaiser, N. S.; Ding, Q.; Jin, S. High-Performance Electrocatalysis Using Metallic Cobalt Pyrite (CoS$_2$) Micro- and Nanostructures. *J. Am. Chem. Soc.* **2014**, 136 (28), 10053−10061.

(17) Hu, C.; Zhang, L.; Zhao, Z.-J.; Li, A.; Chang, X.; Gong, J. Synergism of Geometric Construction and Electronic Regulation: 3D Se-(NiCo)S$_x$/(OH)$_x$ Nanosheets for Highly Efficient Overall Water Splitting. *Adv. Mater.* **2018**, 30 (12), 1705538.

(18) Zhao, H.; Zhu, Y.; Li, F.; Hao, R.; Wang, S.; Guo, L. A Generalized Strategy for the Synthesis of Large-Size Ultrathin Two-Dimensional Metal Oxide Nanosheets. *Angew. Chem., Int. Ed.* **2017**, 56 (30), 8766−8770.

(19) Wu, X.-J.; Huang, X.; Liu, J.; Li, H.; Yang, J.; Li, B.; Huang, W.; Zhang, H. Two-Dimensional CuSe Nanosheets with Microscale Lateral Size: Synthesis and Template-Assisted Phase Transformation. *Angew. Chem., Int. Ed.* **2014**, 53 (20), 5083−5087.

(20) Wang, H.; Wang, H.; Wan, H.; Wu, D.; Chen, G.; Zhang, N.; Cao, Y.; Liu, X.; Ma, R. Ultrathin Nanosheet-Assembled Co−Fe Hydroxide Nanotubes: Sacrificial Template Synthesis, Topotactic Transformation, and Their Application as Electrocatalysts for Efficient Oxygen Evolution Reaction. *ACS Appl. Mater. Interfaces* **2020**, 12 (41), 46578−46587.

(21) Lv, X.; Li, X.; Yang, C.; Ding, X.; Zhang, Y.; Zheng, Y.; Li, S.; Sun, X.; Tao, X. Large-Size, Porous, Ultrathin NiCoP Nanosheets for Efficient Electro/Photocatalytic Water Splitting. *Adv. Funct. Mater.* **2020**, 30 (16), 1910830.

(22) Ding, Y.; Zhang, Z.; Luo, B.; Liao, Q.; Liu, S.; Liu, Y.; Zhang, Y. Investigation on the Broadband Electromagnetic Wave Absorption Properties and Mechanism of Co$_3$O$_4$-Nanosheets/Reduced-Graphene-Oxide Composite. *Nano Res.* **2017**, 10 (3), 980−990.

(23) Shahnaz, T.; Sharma, V.; Subbiah, S.; Narayanasamy, S. Multivariate Optimisation of Cr (VI), Co (III) and Cu (II) Adsorption onto Nanobentonite Incorporated Nanocellulose/Chitosan Aerogel Using Response Surface Methodology. *Journal of Water Process Engineering* **2020**, 36, 101283.

(24) Zhang, M.; de Respinis, M.; Frei, H. Time-Resolved Observations of Water Oxidation Intermediates on a Cobalt Oxide Nanoparticle Catalyst. *Nat. Chem.* **2014**, 6 (4), 362−367.

(25) Lienau, K.; Triana, C. A.; Reith, L.; Siol, S.; Patzke, G. R. Microwave-Hydrothermal Tuning of Spinel-Type Co$_3$O$_4$ Water Oxidation Catalysts. *Front. Chem.* **2020**, 8, 473.

(26) Fan, C. Y.; Zhang, X.-H.; Shi, Y.-H.; Xu, H.-Y.; Zhang, J.-P.; Wu, X.-L. 2D Few-Layer Iron Phosphosulfide: A Self-Buffer Heterophase Structure Induced by Irreversible Breakage of P−S Bonds for High-Performance Lithium/Sodium Storage. *J. Mater. Chem. A* **2019**, 7 (4), 1529−1538.

(27) Hirabayashi, D.; Yoshikawa, T.; Kawamoto, Y.; Mochizuki, K.; Suzuki, K. Characterization and Applications of Calcium Ferrites Based Materials Containing Active Oxygen Species. *Adv. Sci. Technol.* **2006**, 45, 2169−2175.

(28) Ji, X.; Zhang, R.; Shi, X.; Asiri, A. M.; Zheng, B.; Sun, X. Fabrication of Hierarchical CoP Nanosheet@microwire Arrays via Space-Confined Phosphidation toward High-Efficiency Water Oxidation Electrocatalysis under Alkaline Conditions. *Nanoscale* **2018**, 10 (17), 7941−7945.

(29) Grzybek, T. The Influence of the Support Structure on the Iron Distribution for Fe^{3+}-Active Carbon Catalysts. *Fuel* **1990**, 69 (5), 604−607.

(30) Wen, X.; Yang, X.; Li, M.; Bai, L.; Guan, J. Co/CoO$_x$ Nanoparticles Inlaid onto Nitrogen-Doped Carbon-Graphene as a Trifunctional Electrocatalyst. *Electrochim. Acta* **2019**, 296, 830−841.

(31) Liu, Z.; Liu, Y.; Zhong, Y.; Cui, L.; Yang, W.; Razal, J. M.; Barrow, C. J.; Liu, J. Facile Construction of MgCo$_2$O$_4$@CoFe Layered Double Hydroxide Core-Shell Nanocomposites on Nickel Foam for High-Performance Asymmetric Supercapacitors. *J. Power Sources* **2021**, 484, 229288.

(32) Cai, Z.; Na, J.; Lin, J.; Alshehri, A. A.; Alzahrani, K. A.; Alghamdi, Y. G.; Lim, H.; Zheng, J.; Xia, W.; Wang, Z.; Yamauchi, Y. Hierarchical Tubular Architecture Constructed by Vertically Aligned CoS$_2$-MoS$_2$ Nanosheets for Hydrogen Evolution Electrocatalysis. *Chem. - Eur. J.* **2020**, 26 (28), 6195−6204.

(33) Chen, J.; Zhang, Y.; Ye, H.; Xie, J.-Q.; Li, Y.; Yan, C.; Sun, R.; Wong, C. P. Metal−Organic Framework-Derived Co$_x$Fe$_{1−x}$P Nanoparticles Encapsulated in N-Doped Carbon as Efficient Bifunctional Electrocatalysts for Overall Water Splitting. *ACS Appl. Energy Mater.* **2019**, 2 (4), 2734−2742.

(34) Li, M.; Deng, X.; Liang, Y.; Xiang, K.; Wu, D.; Zhao, B.; Yang, H.; Luo, J.-L.; Fu, X.-Z. Co P@NiCo-LDH Heteronanosheet Arrays as Efficient Bifunctional Electrocatalysts for Co-Generation of Value-Added Formate and Hydrogen with Less-Energy Consumption. *J. Energy Chem.* **2020**, 50, 314−323.

(35) Conway, B. E.; Tilak, B. V. Interfacial Processes Involving Electrocatalytic Evolution and Oxidation of H$_2$, and the Role of Chemisorbed H. *Electrochim. Acta* **2002**, 47 (22−23), 3571−3594.

(36) Xu, Y.-F.; Gao, M.-R.; Zheng, Y.-R.; Jiang, J.; Yu, S.-H. Nickel/Nickel(II) Oxide Nanoparticles Anchored onto Cobalt(IV) Diselenide Nanobelts for the Electrochemical Production of Hydrogen. *Angew. Chem.* **2013**, 125 (33), 8708−8712.

(37) Shi, Y.; Zhang, B. Recent Advances in Transition Metal Phosphide Nanomaterials: Synthesis and Applications in Hydrogen Evolution Reaction. *Chem. Soc. Rev.* **2016**, 45 (6), 1529−1541.

(38) Anantharaj, S.; Ede, S. R.; Sakthikumar, K.; Karthick, K.; Mishra, S.; Kundu, S. Recent Trends and Perspectives in Electrochemical Water Splitting with an Emphasis on Sulfide, Selenide, and Phosphide Catalysts of Fe, Co, and Ni: A Review. *ACS Catal.* **2016**, 6 (12), 8069−8097.

(39) Zhou, Q.; Shen, Z.; Zhu, C.; Li, J.; Ding, Z.; Wang, P.; Pan, F.; Zhang, Z.; Ma, H.; Wang, S.; Zhang, H. Nitrogen-Doped CoP Electrocatalysts for Coupled Hydrogen Evolution and Sulfur Generation with Low Energy Consumption. *Adv. Mater.* **2018**, 30 (27), 1800140.

(40) Song, W.; Ren, Z.; Chen, S.-Y.; Meng, Y.; Biswas, S.; Nandi, P.; Elsen, H. A.; Gao, P.-X.; Suib, S. L. Ni- and Mn-Promoted Mesoporous Co$_3$O$_4$: A Stable Bifunctional Catalyst with Surface-Structure-Dependent Activity for Oxygen Reduction Reaction and Oxygen Evolution Reaction. *ACS Appl. Mater. Interfaces* **2016**, 8 (32), 20802−20813.

(41) Zhou, Z.; Zaman, W. Q.; Sun, W.; Cao, L.; Tariq, M.; Yang, J. Cultivating Crystal Lattice Distortion in IrO$_2$ *via* Coupling with MnO$_2$ to Boost the Oxygen Evolution Reaction with High Intrinsic Activity. *Chem. Commun.* **2018**, 54 (39), 4959−4962.

(42) De Koninck, M.; Poirier, S. C.; Marsan, B. Cu$_x$Co$_{3−x}$O$_4$ Used as Bifunctional Electrocatalyst. *J. Electrochem. Soc.* **2006**, 153 (11), A2103.

(43) Liang, Y.; Wang, H.; Diao, P.; Chang, W.; Hong, G.; Li, Y.; Gong, M.; Xie, L.; Zhou, J.; Wang, J.; Regier, T. Z.; Wei, F.; Dai, H. Oxygen Reduction Electrocatalyst Based on Strongly Coupled Cobalt Oxide Nanocrystals and Carbon Nanotubes. *J. Am. Chem. Soc.* **2012**, 134 (38), 15849−15857.

(44) Zhan, K.; Feng, C.; Feng, X.; Zhao, D.; Yue, S.; Li, Y.; Jiao, Q.; Li, H.; Zhao, Y. Iron-Doped Nickel Cobalt Phosphide Nanoarrays

with Urchin-like Structures as High-Performance Electrocatalysts for Oxygen Evolution Reaction. *ACS Sustainable Chem. Eng.* **2020**, *8* (16), 6273−6281.

(45) Jin, S. Are Metal Chalcogenides, Nitrides, and Phosphides Oxygen Evolution Catalysts or Bifunctional Catalysts? *ACS Energy Lett.* **2017**, *2* (8), 1937−1938.

(46) Abouserie, A.; El-Nagar, G. A.; Heyne, B.; Günter, C.; Schilde, U.; Mayer, M. T.; Stojkovikj, S.; Roth, C.; Taubert, A. Facile Synthesis of Hierarchical CuS and $CuCo_2S_4$ Structures from an Ionic Liquid Precursor for Electrocatalysis Applications. *ACS Appl. Mater. Interfaces* **2020**, *12* (47), 52560−52570.

(47) Qiu, Y.; Jia, Q.; Yan, S.; Liu, B.; Liu, J.; Ji, X. Favorable Amorphous−Crystalline Iron Oxyhydroxide Phase Boundaries for Boosted Alkaline Water Oxidation. *ChemSusChem* **2020**, *13* (18), 4911−4915.

(48) Liu, Z.; Wang, G.; Zhu, X.; Wang, Y.; Zou, Y.; Zang, S.; Wang, S. Optimal Geometrical Configuration of Cobalt Cations in Spinel Oxides to Promote Oxygen Evolution Reaction. *Angew. Chem., Int. Ed.* **2020**, *59* (12), 4736−4742.

(49) Liao, K.; Chen, S.; Wei, H.; Fan, J.; Xu, Q.; Min, Y. Micropores of Pure Nanographite Spheres for Long Cycle Life and High-Rate Lithium−Sulfur Batteries. *J. Mater. Chem. A* **2018**, *6* (45), 23062−23070.

(50) Mandal, M.; Kruk, M. Surfactant-Templated Synthesis of Ordered Silicas with Closed Cylindrical Mesopores. *Chem. Mater.* **2012**, *24* (1), 149−154.

(51) Wang, T.; Zhang, Y.; Wang, Y.; Zhou, J.; Wu, L.; Sun, Y.; Xu, X.; Hou, W.; Zhou, X.; Du, Y.; Zhong, W. Alumina-Supported CoPS Nanostructures Derived from LDH as Highly Active Bifunctional Catalysts for Overall Water Splitting. *ACS Sustainable Chem. Eng.* **2018**, *6* (8), 10087−10096.

(52) Sun, C.; Dong, Q.; Yang, J.; Dai, Z.; Lin, J.; Chen, P.; Huang, W.; Dong, X. Metal−Organic Framework Derived $CoSe_2$ Nanoparticles Anchored on Carbon Fibers as Bifunctional Electrocatalysts for Efficient Overall Water Splitting. *Nano Res.* **2016**, *9* (8), 2234−2243.

(53) Hou, Y.; Lohe, M. R.; Zhang, J.; Liu, S.; Zhuang, X.; Feng, X. Vertically Oriented Cobalt Selenide/NiFe Layered-Double-Hydroxide Nanosheets Supported on Exfoliated Graphene Foil: An Efficient 3D Electrode for Overall Water Splitting. *Energy Environ. Sci.* **2016**, *9* (2), 478−483.

(54) Tsai, H.-C.; Vedhanarayanan, B.; Lin, T.-W. Freestanding and Hierarchically Structured Au-Dendrites/3D-Graphene Scaffold Supports Highly Active and Stable Ni_3S_2 Electrocatalyst toward Overall Water Splitting. *ACS Appl. Energy Mater.* **2019**, *2* (5), 3708−3716.

(55) Chen, Y.; Xu, S.; Zhu, S.; Jacob, R. J.; Pastel, G.; Wang, Y.; Li, Y.; Dai, J.; Chen, F.; Xie, H.; Liu, B.; Yao, Y.; Salamanca-Riba, L. G.; Zachariah, M. R.; Li, T.; Hu, L. Millisecond Synthesis of CoS Nanoparticles for Highly Efficient Overall Water Splitting. *Nano Res.* **2019**, *12* (9), 2259−2267.

(56) Deng, S.; Zhong, Y.; Zeng, Y.; Wang, Y.; Wang, X.; Lu, X.; Xia, X.; Tu, J. Hollow $TiO_2@Co_9S_8$ Core−Branch Arrays as Bifunctional Electrocatalysts for Efficient Oxygen/Hydrogen Production. *Adv. Sci.* **2018**, *5* (3), 1700772.

(57) Liu, D.; Lu, Q.; Luo, Y.; Sun, X.; Asiri, A. M. $NiCo_2S_4$ Nanowires Array as an Efficient Bifunctional Electrocatalyst for Full Water Splitting with Superior Activity. *Nanoscale* **2015**, *7* (37), 15122−15126.

(58) Xue, Y.; Zuo, Z.; Li, Y.; Liu, H.; Li, Y. Graphdiyne-Supported $NiCo_2S_4$ Nanowires: A Highly Active and Stable 3D Bifunctional Electrode Material. *Small* **2017**, *13* (31), 1700936.

(59) Wu, N.; Lei, Y.; Wang, Q.; Wang, B.; Han, C.; Wang, Y. Facile Synthesis of FeCo@NC Core−Shell Nanospheres Supported on Graphene as an Efficient Bifunctional Oxygen Electrocatalyst. *Nano Res.* **2017**, *10* (7), 2332−2343.